The 8th European Congress on Computational Methods in Applied Sciences and Engineering
ECCOMAS Congress 2022
5 – 9 June 2022, Oslo, Norway

FORMING EFFECTS ON HIGH-CYCLE FATIGUE IN AN ALUMINUM SHEET STRUCTURE USING THE OTTOSEN-STENSTRÖM-RISTINMAA MODEL

SIGBJØRN TVEIT, AASE REYES AND EMRAH ERDURAN

Department of Built Environment
Oslo Metropolitan University
Post box 4, St. Olavs plass, NO-0130 Oslo, Norway
e-mail: sigbjorn.tveit@oslomet.no, aase.reyes@oslomet.no, emrah.erduran@oslomet.no
www.oslomet.no

Key words: Metal Sheet Forming, High-Cycle Fatigue, Aluminum, Finite Element Analysis.

Abstract. In this paper a multi-stage numerical analysis is presented with the aim to investigate effects of forming on the high-cycle fatigue performance of a deep-drawn aluminum sheet structure for use in a floating photovoltaic system. Forming simulations of a subsection of the full geometry are performed in a realistic two-step drawing-springback cycle. A simplified global analysis of service load response is performed to obtain displacements at the submodel boundary, that are used to generate boundary conditions for a local service load analysis. The local analysis is then performed on three different models of the subsection: (I) excluding forming effects, (II) including effects of thinning, and (III) including effects of thinning and residual stresses. The critical location with respect to the fatigue limit criterion in the Ottosen-Stenström-Ristinmaa high-cycle fatigue model was identified for case (I), and this location was used to compare the different models to assess effects of forming on high-cycle fatigue performance. Furthermore, the dynamic friction coefficient f_d, and the isotropic-kinematic mixing coefficient B were varied in order to investigate their respective effects.

1 INTRODUCTION

For solar power to significantly contribute to covering the global energy demand, vast areas dedicated to production are required. Furthermore, to reduce stress on existing power grids and infrastructure, production locations should be placed as close as possible to the areas of consumption. However, in densely populated districts where energy consumption is large, such zones are often prioritized for agricultural purposes, etc. With the rapidly increasing global demand for non-fossil and sustainable energy, technological, innovative and scalable solutions to utilize renewable resources such as solar energy, are currently subject to extensive research.

Utilizing previously unused area for power production, the global potential of floating photovoltaic (FPV) power has with conservative assumptions been estimated to 400 GW, which equals the capacity of the 2017 cumulated installed solar energy plants [1]. While FPV has been mostly restricted to the tranquil environments of freshwater reservoirs such as lakes and dams, near-shore ocean territories are now gaining attention as potential sites for marine floating solar power generation. With 70% of the world's major cities situated in the immediate vicinity to

the sea or other large bodies of water, technology that enables solar power production in such locations allows the possibility of drastically scaling up production capacity.

A challenge with expanding the attention to also include in-shore marine environments is the increased service loads associated with the wave loads. As floating structures are typically subject to a high number of stress cycles from wave loads, the repeated loads might cause high-cycle fatigue (HCF) failure at stress ranges far below the material's static capacity. Furthermore, high-cycle fatigue in metals is known to depend on certain superimposed mean stress configurations.

During forming, the ductile aluminum undergoes large plastic and small elastic deformations. While the plastic strains are permanent, the elastic strains are reversed upon release of the drawing tools. This yields a configuration at equilibrium where some elastic strains are internally constrained from returning to the stress-free state [2], producing a state of residual stress.

The importance of incorporating effects from manufacturing in such analysis was emphasized by Hariharan and Prakash [3], in their review article on challenges integrating effects of forming in fatigue life predictions.

Facchinetti et al. [4] investigated the effects of forming on the HCF performance of a pseudo Mac-Pherson front axle. In the study, HCF computations by the Dang-Van approach [5] were carried out considering different forming effects, including those from thinning, plastic strains and residual stresses. By including all forming effects in the fatigue assessment, safety factors were reduced by more than 15% compared to the idealized case. The plastic behavior of the steel sheet was modelled using linear isotropic hardening, and so the Bauschinger effect [6], and its influences on the residual stress levels, were not considered.

In this paper, a multi-stage numerical analysis is presented with the aim of investigating the effects of forming on HCF in a formed aluminum sheet float component designed by the FPV technology provider Sunlit Sea AS. Using a non-quadratic isotropic yield surface and an associated isotropic-kinematic exponential hardening law, metal sheet forming analyses in LS-DYNA are conducted to obtain predictions of thinning and residual stress fields in the manufactured components. A simplified global analysis of the full structure's service load response is conducted to obtain boundary conditions for a local service load response analysis of the formed sheet. From this, a constant amplitude load case that serves as a simplified representation of service wave loads is assessed in the HCF framework proposed by Ottosen et al. [7] in a MATLAB implemented forward Euler scheme for time integration of the model's history variables.

In addition to the effects of thinning and residual stresses from forming on HCF, the influence of two forming parameters, namely the dynamic friction coefficient f_d, and the isotropic-kinematic mixing coefficient B is further investigated.

2 FPV STRUCTURE

In the FPV plant, several floating units are connected in a large matrix that is held in position by a mooring system. Each FPV unit is mounted directly on to a float, which consists of two identical aluminum sheet components (cf. Fig. 1) that are welded together, back-to-back, with sealed off edges to generate a buoyant pontoon. The components are produced in a two-stage forming operation, where 1.5 mm thick rolled AA5083-H111 sheets are deep-drawn into

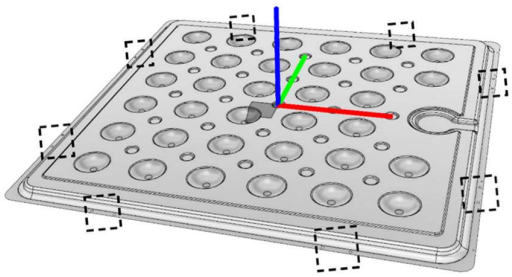

Figure 1: The red, green and blue coordinate axes respectively correspond to the x-, y- and z-axes of the global coordinate system. The dashed rectangles indicate locations of connectors, and the darkened area displays the submodel assessed in Section 6.2 and 6.3. The geometry was provided by Sunlit Sea AS.

a cupcake tray-like shape. Aside from providing a stable support in rough weather conditions, the aluminum structure acts as a thermal bridge between the panels and the cool sea water, increasing the efficiency of the PV cells.

In the multi-stage analyses presented in this paper, the global model (1880 x 1880 mm full structure) and the local model (130 x 130 mm submodel) refer to the same global Cartesian coordinate system displayed in Fig. 1.

3 PLASTICITY MODEL

In the current work, a mixed isotropic-kinematic hardening model that follows a power law dependency on plastic strain is assumed:

$$\sigma_Y = k\left(\bar{\varepsilon}_0 + \bar{\varepsilon}_p\right)^n \tag{1}$$

Here, σ_Y is the flow stress, k is the strength coefficient, $\bar{\varepsilon}_0$ is the effective strain at the onset of yield, $\bar{\varepsilon}_p$ is the effective plastic strain, and n is the hardening exponent.

The plastic strain increment follows the associate flow rule, and the mixing coefficient $0 \leq \mathrm{B} \leq 1$ defines the respective contributions to isotropic $(\mathrm{B} = 0)$ and kinematic $(\mathrm{B} = 1)$ hardening. The kinematic backstress tensor $\boldsymbol{\alpha}$ describes the deviatoric center of the of the yield locus. For the complete mathematical description of the mixed hardening model, cf. [8].

The yield criterion is defined according to the non-quadratic Hershey-Hosford formulation [9,10], which may be written as function of the deviatoric stress tensor $\boldsymbol{s} = \boldsymbol{\sigma} - \mathbf{I}\, tr(\boldsymbol{\sigma})/3$, where $\mathbf{I}$ is the identity tensor. Introducing a plastic backstress-modified deviatoric stress tensor, $\hat{\boldsymbol{s}} = \boldsymbol{s} - \boldsymbol{\alpha}$, the Hershey-Hosford equation is written in principle components as

$$|\hat{s}_1 - \hat{s}_2|^m + |\hat{s}_2 - \hat{s}_3|^m + |\hat{s}_3 - \hat{s}_1|^m = 2\hat{\sigma}_{hh}{}^m \tag{2}$$

where m is the flow potential exponent, and $\hat{\sigma}_{hh}$ is the Hershey-Hosford effective stress. For $m = 2$ and $m = 4$, the formulation reduces to the von Mises criterion, while for $m = 1$ and $m = \infty$ it reduces to the Tresca criterion. The appropriate value of this floating parameter may be fitted to agree with experimental observations or crystal-plasticity based simulations, although the conformity of $m = 8$ for face-centered cubic (FCC) materials, such as aluminum, is well established.

4 HIGH-CYCLE FATIGUE MODEL

The Ottosen-Stenström-Ristinmaa HCF model [7] introduces a continuous accumulative damage function, whose evolution is dictated by the elastic stress history. Inspired by plasticity theory, the model proposes an endurance surface in stress space that separates a safe domain, where fatigue damage cannot evolve, from an unsafe domain where fatigue damage may accumulate if the stress state is moving away from the endurance surface in the stress space. The locus moves in the deviatoric stress space according to an endurance backstress tensor $\boldsymbol{\mu}$, which should not be confused with the plastic backstress tensor $\boldsymbol{\alpha}$ that dictates yield surface translation due to kinematic plastic strain hardening. The endurance function β defines the endurance limit when $\beta = 0$, and is expressed as

$$\beta = \frac{1}{S_o}(\hat{\sigma}_{vm} + AI_1 - S_o) \tag{3}$$

where A is a positive dimensionless parameter which describes hydrostatical dependency, $I_1 = tr(\boldsymbol{\sigma})$ is the first stress tensor invariant, and S_o is the endurance limit for completely reversed stress cycles ($R = \sigma_{min}/\sigma_{max} = -1$). Furthermore, $\hat{\sigma}_{vm}$ is the endurance backstress-modified von Mises effective stress, which may be expressed as

$$\hat{\sigma}_{vm} = \left[\frac{3}{2}(\boldsymbol{s} - \boldsymbol{\mu}) : (\boldsymbol{s} - \boldsymbol{\mu})\right]^{1/2} = \sqrt{\frac{3}{2}}\|\boldsymbol{s} - \boldsymbol{\mu}\| \tag{4}$$

Here, $\boldsymbol{s}$ is the deviatoric stress tensor, and the colon operator denotes the double dot product $\boldsymbol{A}:\boldsymbol{B} = tr(\boldsymbol{A}\boldsymbol{B}^T)$. It follows from Eq. (3) and (4) that $\beta < 0$ corresponds to stress states inside the endurance locus, while $\beta = 0$ represents stress states on its surface. Opposed to plasticity theory, where the implicit function is restricted to values ≤ 0, the endurance function β may also take on values > 0, corresponding to stress states located outside the endurance locus in stress space. It is worth noting that for cyclic proportional stress paths, the endurance backstress eventually reaches a stable configuration that reduces Eq. (3) to the well-known fatigue limit criterion of Sines [11].

In the OSR HCF model, both the endurance backstress μ, and the fatigue damage is assumed to accumulate whenever the stress state is located outside the endurance locus ($\beta > 0$) and moving away from it ($d\beta > 0$). The backstress evolution equation is written on incremental form as

$$d\boldsymbol{\mu} = d\beta C(\boldsymbol{s} - \boldsymbol{\mu}) \tag{5}$$

where C is a positive and dimensionless material parameter. Furthermore, the damage scalar D that exists in the continuous domain from 0 (virgin state) to 1 (fatigue failure), if assumed independent of the current amount of damage, may be expressed on incremental form as

$$dD = d\beta K exp(L\beta) \tag{6}$$

with the positive dimensionless material parameters K and L, and with the restriction $dD \geq 0$.

With this, the continuous-time model presented provides a unified formulation of fatigue limits and damage accumulation for arbitrary stress histories, where the cycle-counting methods used in conventional models are replaced by the integration of Eq. (5) and (6) though time.

5 MATERIAL

In this paper we have considered sheets of AA5083-H111 rolled to 1.5 mm thickness. The alloy is commonly used for marine structures due to its high strength and good resistance to the chemical environment of seawater. For rolled aluminum alloy sheets of a specific alloy and temper, properties of the as-delivered products may vary depending on several factors in the production process, including exact chemical composition and amount of work hardening. When performing simulations with the aim to make accurate predictions, it is preferable to use experimental data from tests on the specific supplied product when calibrating model parameters. However, in this preliminary study, model parameters were fitted to data reported in the literature for equivalent or similar materials, and summarized in Table 1.

The hardening coefficients for AA5083-H111 were obtained from the uniaxial tensile test results by Janbakhsh et al. [12], cf. Fig. 2(a). In the experimental study, data presented for 1 mm thick dog-bone specimens oriented parallel to the sheet's rolling direction was used to fit the exponential hardening law presented in Eq. (1).

For parameter calibration of the OSR model, HCF data of AA5083-H11 presented by Sidhom et al. [13] was used. In the study, a four-point bending test was performed on 10 mm thick rectangular plates (60 x 300 mm) at two different stress ratios, $R = 0.1$ and $R = 0.5$. The graphical S-N data (stress amplitude σ_a vs. number of cycles at failure N_f) was digitized and used along with the 50% probable nominal fatigue limits taken at 2×10^6 cycles, as presented in the article. Parameter A was calculated directly from the nominal fatigue limits of 142 MPa ($R = 0.1$) and 112 MPa ($R = 0.5$) and was further used to obtain S_0 by extrapolation to the zero mean stress state. S-N data for $R = 0.1$ at equal stress levels was averaged to create three distinct datapoints for calibration of the remaining parameters C, K and L, where the error function proposed by Ottosen et al. [7] was minimized using a genetic algorithm optimization method in MATLAB. Fig. 2(b) displays the experimental S-N data as presented by Sidhom et al. [13], along with the averaged quantities used for calibration, and the predicted S-N curves for $R = 0.1$ and 0.5. Note that the predicted curve for $R = 0.5$ displays fair agreement with the corresponding datapoints, although they were not used in the parameter fitting.

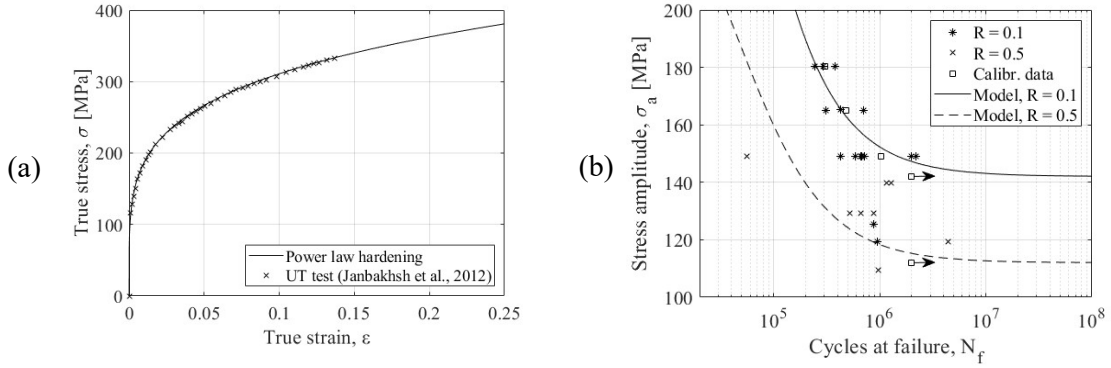

Figure 2: (a) The fitted power law hardening curve and stress-strain data from UT test specimens oriented longitudinal to the sheet's rolling direction, reproduced from [12]. (b) S-N diagram displaying the parameter fit for AA5083-H11. The data presented in [13] includes the scattered datapoints (stars and crosses), and the 50% probable nominal fatigue limits at $R = 0.1$ (upper) and $R = 0.5$ (lower) represented by arrowed squares. The squares represent the averaged $R = 0.1$ datapoints used in the numerical calibration of C, K and L.

Table 1: Model parameters for AA5083

Elastic/mechanical properties [14]	E [MPa]	ν	ρ [kg/m^3]		
	72000	*0.33*	*2650*		
Plasticity parameters (based on [12])	k [MPa]	$\bar{\varepsilon}_0$ [%]	n	m	
	517.3	*0.258*	*0.221*	*8*	
OSR parameters (based on [13])	A	S_0 [MPa]	C	K	L
	0.185	*174*	*2.72×10^5*	*0.726*	*3.55×10^{-2}*

6 NUMERICAL ANALYSIS

6.1 Forming simulation

An attempt was made to realistically simulate the evolution of deformations, stresses, and strains during the forming in manufacturing, by use of the commercial finite element (FE) analysis software LS-DYNA. The process was simulated in four consecutive steps: 1a) drawing of small cups, 1b) first springback, 2a) drawing of large cups, and 2b) second springback (cf. Table 2). We took advantage of the repeated geometry by modeling a 130 x 130 mm submodel of the full structure. The top and bottom surface of the 3D design geometry was used to generate tool parts for the two drawing steps (cf. Fig. 3(a). for assembly of FE parts).

Global symmetry constraints were applied to the four planes enclosing the submodel domain, and a one-way surface-to-surface contact rule was defined to dictate interaction between the tools and the blank. To provide satisfactory spatial discretization, an initially uniform mesh of 20 by 20 shell elements (thickness 1.5 mm) was equipped with a five-level h-refinement criterion considering the total rotation relative to surrounding shells, with a threshold of five degrees per level.

Table 2: Model specs of the forming simulation model

	Stage 1 (small cup)			Stage 2 (large cup)		
a) Drawing						
Time integration	*Explicit*			*Explicit*		
Punch travel [mm]	*5.0*			*38.5*		
Duration [s]	*1.0*			*2.0*		
Element type	*Belytschko-Tsay shell, NIP = 7*			*Belytschko-Tsay shell, NIP = 7*		
	Blank	Punch	Die	Blank	Punch	Die
Num. of elements (start)	*400*	*842*	*926*	*3496**	*4918*	*4993*
Num. of elements (end)	*3496**			*5728**		
b) Springback						
Time integration	*Implicit (static)*			*Implicit (static)*		
Element type	*Full integration shell, NIP = 7*			*Full integration shell, NIP = 7*		
	Blank			Blank		
Num. of elements	*3496**			*5728**		

*For B $= 0.25$ and $f_d = 0.1$

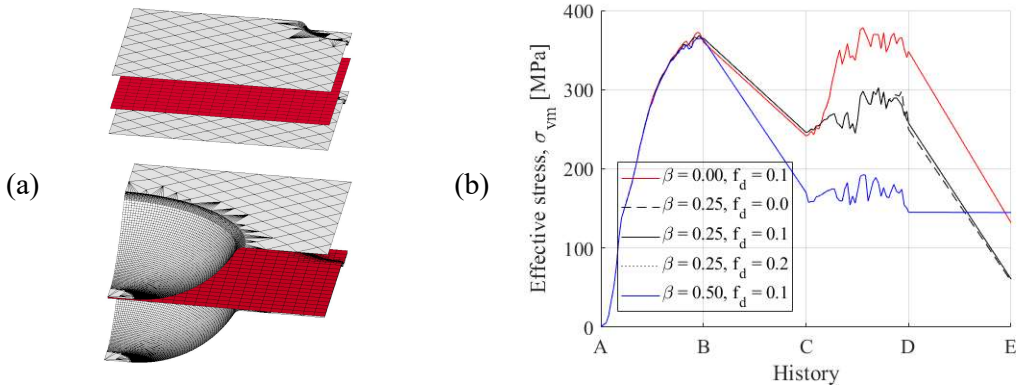

Figure 3: (a) Assembly of FE parts for the first (upper) and second (lower) drawing of the formability simulation. The tools (grey) are modelled as rigid parts, while the blank (red) obeys the constitutive laws presented in 2.1. (b) Effective stress histories throughout the different stages of the forming simulations in a critical location for fatigue failure, cf. Section 6.3 and Fig. 4: 1a) Drawing of small cups (A-B), 1b) first springback (B-C), 2a) drawing of large cups (C-D), and 2b) second springback (D-E). Curves representing B $= 0.25$, $f_d = 0.1$ and 0.2 coincide and are indistinguishable.

An explicit central difference time-integration scheme was used to ensure robustness for the highly non-linear drawing analyses, while springback was simulated in a static implicit analysis. The explicit drawing steps employed reduced integration Belytschko-Tsay shell elements, while the implicit steps were conducted with full integration shells (respectively *ELFORM 2* and *16* in LS-DYNA [15]), with seven through-thickness integration points (NIP).

With the aim to study their influence on HCF, forming simulations were carried out while varying two presumably independent parameters: the dynamic coefficient of friction ($f_d = 0.0$, 0.1 and 0.2), and the isotropic-kinematic mixing coefficient ($B = 0.00$, 0.25 and 0.50). Fig. 3(b) displays von Mises effective stress histories for the five different parameter couples in a critical location for fatigue failure (cf. Section 6.3).

6.2 Analysis of service load response

Based on the idealized design geometry, an FE model of the full structure was established with 1.5 mm thick fully integrated shell elements. To limit computational time, the structure was spatially discretized with a mesh that is coarse compared to the h-refinement adapted mesh from the forming simulation. See Table 3 for further details.

In this preliminary study, the deformation mode of unconstrained tension in the global x-direction was simulated. The load was applied as a prescribed displacement at the connector locations on the sides parallel to the global y-direction, while the connectors on the sides parallel to the x-direction were left unconstrained, cf. Fig. 4. The magnitude of the prescribed displacement (2.5 mm) was chosen by limiting the maximum effective stress level below the material's initial yield stress limit σ_0, anywhere in the full structure.

From the global analysis model, in-plane displacements at the location of the submodel boundary were stored and simplified, and later applied as boundary conditions in the local analysis. The simplification involved calculating the length change of the submodel domain in the x- and y-directions, as well as their respective average values, cf. Fig. 5(a) and (b).

Table 3: Model specs of global and local service load analysis models

a) Global service load model	
Time integration	*Implicit (static)*
Element type	*Full integration shell, NIP = 7*
Num. of elements	*45 393 (221 in submodel region)*
Element size at critical radii	*~ 5.0 mm*
b) Local service load model	
Time integration	*Implicit (static)*
Element type	*Full integration shell, NIP = 7*
Num. of elements	*5728**
Element size at critical radii	*~ 0.4 mm*

*For $\beta = 0.25$ and $f_d = 0.1$

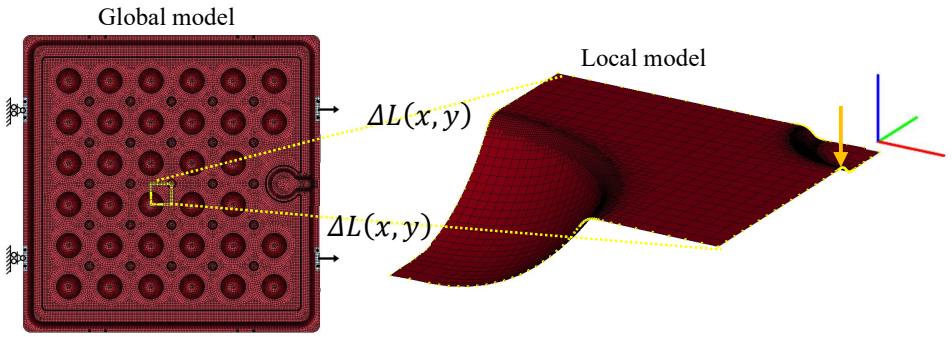

Figure 4: Boundary conditions of global and local analysis models. The orange arrow indicates the critical location for analysis case (I) (cf. Section 6.3), and the coordinate system refers to the global origin, with the red, green and blue axes respectively referring to the x-, y- and z-direction.

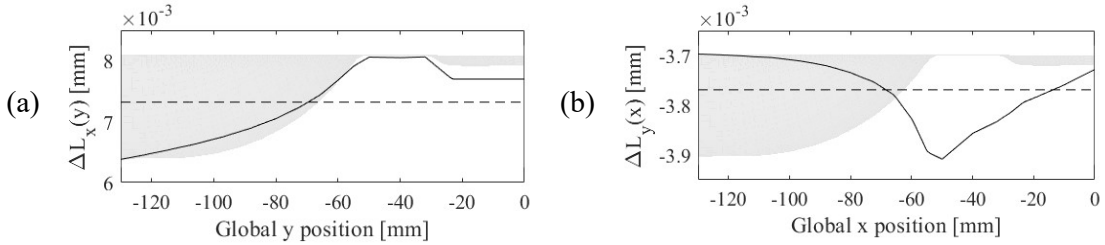

Figure 5: (a) Change of length of submodel in x direction, and (b) change of length of submodel in y-direction, during global tensile deformation in x-direction. The silhouettes indicate projections of the structure geometry to abscissa entities.

The final configuration of the forming analysis described in Section 6.1 was used to generate two versions of the submodel for the local service load response analysis: one that included thinning due to forming, and one that did not – both disregarding residual stresses. The local analyses were then conducted by applying the averaged elongation in x- direction and average contraction in y- direction, while keeping the remaining symmetric boundary conditions from the forming analysis.

6.3 Fatigue analysis

A forward Euler scheme for the explicit integration of history variables in the OSR model was implemented in MATLAB. The program takes the stress tensor history in one material point as input, and by expressing the variation of stress tensor components as harmonic functions, storage of entire stress history data is avoided.

$R = -1$ harmonic fatigue loading stress histories were generated from the local analysis, assuming tension-compression symmetry of the service loads response. To evaluate how forming influences the fatigue resistance, three categories of harmonic stress histories were generated: (I) excluding forming effects, (II) including effects of thinning, and (III) including effects of thinning and residual stresses. While (I) and (II) were taken directly from the local service load analysis results, (III) was obtained by superimposition of results from (II) and the final stress configurations of the forming simulations.

The critical location in case (I) with respect to fatigue failure in the OSR/Sines framework was located. For proportional stress histories without superimposed mean stress, the critical location is identified by simple evaluation of the spatial extremal of the endurance function value in the tensile and compressive states. It was in the present case identified on the top surface of the structure, near the edge of the small cup, where the maximums of the effective stress $\hat{\sigma}_{vm}$ and the first stress tensor invariant I_1 coincided in the tensile state. The location was used to make comparisons between the three cases, to evaluate the effects of forming on HCF resistance. As the fatigue limit was not exceeded in any of the three cases, safety factors with respect to the Sines fatigue limit criterion were found by determining the stress tensor amplitude scale factors s_a that caused fatigue damage accumulation until failure in each case.

To extend the comparison beyond cases that reduce to the Sines fatigue limit criterion, a scale factor $s_a = 25$ (larger than the highest critical scale factor in all cases, but still within the regime of material linearity and high-cycle fatigue in the submodel domain), was applied to calculate the number of cycles at failure under these conditions. In Table 4, critical scale factors, and the number of cycles at failure for $s_a = 25$ are displayed along with the mean values of the first stress tensor invariant I_1 and shell thickness after forming, in the same location. Fig. 6(a) and (b) displays the effective stress histories, and the accumulation of the fatigue damage D at the location used for comparison.

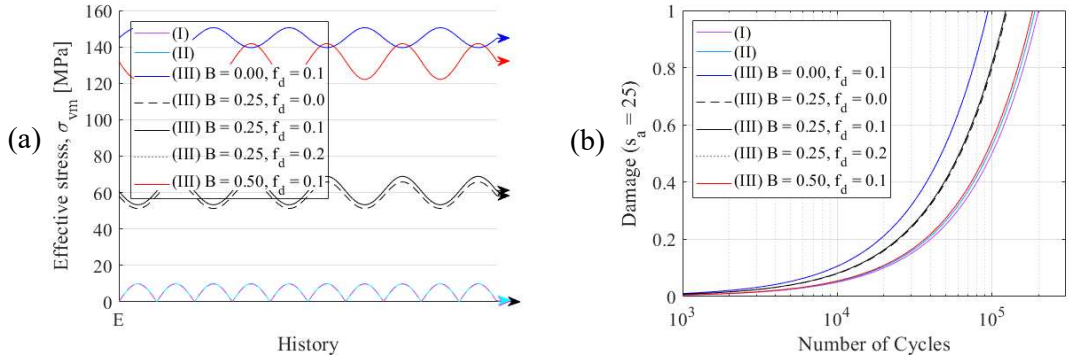

Figure 6: Results from critical location of case (I) (cf. Fig. 4). (a) Effective stress histories of fatigue analysis. (b) Fatigue damage accumulation histories for stress tensor amplitude scale factors $s_a = 25$. In both (a) and (b), curves representing (III) B $= 0.25, f_a = 0.1$ and 0.2 coincide and are indistinguishable.

Table 4: Fatigue analysis results in reference point obtained from critical location (cf. Fig. 4.a) of case (I)

	Critical scale factor $s_{a,cr}$	Cycles at failure $N_{f,25}$	Mean first invariant of $\boldsymbol{\sigma}$ $I_{1,m}$ [MPa]	Shell thickness t [mm]
(I) No forming				
($B = 0.25, f_d = 0.1$)	*17.699*	*199 475*	*0.00*	*1.500*
(II) Thinning				
($B = 0.25, f_d = 0.1$)	*17.461*	*189 592*	*0.00*	*1.378*
(III) Thin. & residual stress				
$B = 0.00, f_d = 0.1$	*13.832*	*94 271*	*200.5*	*1.375*
$B = 0.25, f_d = 0.0$	*15.359*	*124 847*	*112.9*	*1.378*
$B = 0.25, f_d = 0.1$	*15.241*	*122 723*	*119.8*	*1.378*
$B = 0.25, f_d = 0.2$	*15.241*	*122 723*	*119.8*	*1.378*
$B = 0.50, f_d = 0.1$	*17.345*	*183 236*	*-2.070*	*1.381*

7 DISCUSSION AND CONCLUDING REMARKS

In this paper, a multi-stage numerical analysis was performed with the aim to investigate effects of forming on HCF performance of a deep-drawn aluminum sheet structure for use in a FPV plant.

The current study focuses on the assessment of a symmetric submodel in the periodic geometry, located near the center of the float component. A simulation of the forming process was performed in a realistic two-step drawing springback cycle. A simplified global analysis of the full structure's service load response was carried out, and the displacements at the submodel boundary were used to generate boundary conditions for a local service load response analysis. By superposition of results from the forming simulation and the local service load analysis, three different stress histories were obtained for analysis of HCF: (I) Excluding forming effects, (II) Including effects of thinning, and (III) Including effects of thinning and residual stress. The critical location with respect to the fatigue limit criterion used in the OSR/Sines model was identified for case (I), and this location was used to compare the different models in order to assess the effects of forming on HCF performance. Furthermore, two parameters, namely the dynamic friction coefficient f_d, and the isotropic-kinematic mixing coefficient B were varied in order to further investigate their respective effects.

The HCF capacity in the assessed location was distinctly influenced by the forming effects, although the fatigue limit criterion was not exceeded in any of the assessed cases. Relative to the model that excluded forming effects, the critical amplitude scale factor $s_{a,cr}$ for the OSR/Sines fatigue limit criterion was reduced with 22% in the most severe case. When employing a constant amplitude scale factor $s_a = 25$ that exceeded the fatigue limit in all cases, the number of cycles at failure $N_{f,25}$ in the most severe case was reduced to less than half of the reference model that excluded forming effects.

Although the thickness reduction in the assessed location was never less than 8% for any of the parameter couples, $s_{a,cr}$ and $N_{f,25}$ were only reduced respectively by 1% and 5%, when the thinning effect alone was included.

The dynamic friction coefficient f_d had negligible influence on the results in both forming

and fatigue in this study. The residual stress and thinning after forming for $f_d = 0.1$ and $f_d = 0.2$ (at $B = 0.25$) were indistinguishable in the location where the fatigue analysis was conducted, and thus the presented results are identical for the two cases.

From a qualitative evaluation of the forming simulation results, the magnitude of predicted residual hydrostatic pressure at the surfaces of the formed component was generally dependent on the isotropic-kinematic mixing coefficient B. In the location subject to fatigue analysis, the residual component of I_1 was reduced from 200.5 MPa at $B = 0.0$ (fully isotropic) to -2.070 MPa at $B = 0.5$. With the OSR fatigue model employing an endurance function with linear dependency on I_1, the present model predicts that this dependency also applies to HCF.

The results presented in this paper further emphasize the importance of considering effects of residual stresses when assessing HCF performance of formed structures. Further research on this topic could include validation of sophisticated models to predict distributions and magnitudes of residual stresses in formed components, with emphasis on the isotropic-kinematic hardening formulation.

Several simplifications were made in this preliminary study, and the presented work has several limitations, including but not limited to the following:

- Only one region of the structural component was assessed.
- The load history was significantly simplified.
- A simplified method to transfer loads from the global to local model was used.
- Effects of stress gradients, surface roughness, welding and plastic anisotropy were neglected.
- Data reported in the literature for similar but not equivalent materials to the one used in the real structure was used to calibrate material models.

REFERENCES

[1] World Bank Group *Where sun meets water : Floating solar market report - executive summary (english)*, (2018).

[2] Marciniak, Z., Duncan, J.L., and Hu, S.J. *Mechanics of sheet metal forming.* Butterworth-Heinemann, (2002).

[3] Hariharan, K. and Prakash, R.V. Integrating effect of forming in fatigue life prediction: Review of present scenario and challenges. *Pros. Inst. Mech. Eng. B: J. Eng. Manfc* (2012) **226**: 967-979.

[4] Facchinetti, M.L., Weber, B., Doudard, C., and Calloch, S. Taking into account the forming process in fatigue design computations. *Fatigue Design 2007: Recueil des Conferences Proceedings* (2008).

[5] Dang-Van, K. *Macro-micro approach in high-cycle multiaxial fatigue.* ASTM International, (1993).

[6] Vormwald, M. Fatigue of constructional steel s460 under complex cyclic stress and strain sequences. *Proc. Engng* (2011) **10**: 270-275.

[7] Ottosen, N.S., Stenstrom, R., and Ristinmaa, M. Continuum approach to high-cycle fatigue modeling. *Int. J. Fatg* (2008) **30**: 996-1006.

[8] Livermore Software Technology *Ls-dyna® theory manual*. (2019).

[9] Hershey, A.V. The elasticity of an isotropic aggregate of anisotropic cubic crystals. *J. App. Mec.* (1954) **21**: 236-240.

[10] Hosford, W.F. A generalized isotropic yield criterion. *J. App. Mec.* (1972) **39**: 607-609.
[11] Sines, G. *Failure of materials under combined repeated stresses with superimposed static stresses*. University of California at Los Angeles (1955).
[12] Janbakhsh, M., Djavanroodi, F., and Riahi, M. Utilization of bulge and uniaxial tensile tests for determination of flow stress curves of selected anisotropic alloys. *Proc. Inst. Mec. Eng. L: J Mat.: Desg. Applictn* (2013) **227**: 38-51.
[13] Sidhom, N., Laamouri, A., Fathallah, R., Braham, C., and Lieurade, H.P. Fatigue strength improvement of 5083 H11 Al-alloy I-welded joints by shot peening: Experimental characterization and predictive approach. *Int. J. Fat.* (2005) **27**: 729-745.
[14] AZoNetwork *Aluminium alloys - aluminium 5083 properties, fabrication and applications*. (2005) www.azom.com/article.aspx?ArticleID=2804 (Accessed July 8th, 2022).
[15] Livermore Software Technology *Ls-dyna® keyword user's manual*. Vol. I, (2020).
[16] Lee, J., Park, S.-Y., and Choi, B.-H. Evaluation of fatigue characteristics of aluminum alloys and mechanical components using extreme value statistics and C-specimens. *Metals* (2021) **11**: 1915-1926.